Electronic Supplementary Information (ESI)

Dry-processed thick electrode design with porous conductive agent enabling 20 mA h cm^{-2} for high-energy-density lithium-ion battery

*Hyeseong Oh, Gyu-Sang Kim, Jiyoon Bang, San Kim, and Kyeong-Min Jeong**

*Corresponding author. E-mail: kmjeong@unist.ac.kr

Experimental Sections/Methods

Dry Electrode Fabrication

All dry-processed thick cathodes were fabricated in 100 g batches with a weight ratio of A/B/C = $98.5-x/1.5/x$ (x = conductive agent wt%). In the lamination process, free-standing electrode films were laminated onto the carbon-coated Al current collector (Al 15 μm + C 1 μm). The electrodes with an areal capacity of 10 mA h cm^{-2} were produced with a loading level of 50–55 mg cm^{-2} and a composite density range of 3.65–3.83 g cm^{-3}. The ultrathick electrodes, with areal capacities of 15 and 20 mA h cm^{-2}, maintained a composite density of 3.65 ± 0.02 g cm^{-3}. Owing to the differences in the specific surface area and porosity among the conductive agents, there were variations in the composite density for the same content (2 wt%). The composite densities by the conductive agents showed the following trend: CNT (3.83 g cm^{-3}) > SP (3.79 g cm^{-3}) > DB (3.73 g cm^{-3}) > graphene (3.70 g cm^{-3}) > KB (EC-300J, 3.67 g cm^{-3}) > KB (EC-600JD, 3.65 g cm^{-3}). The dry-processed thick electrodes were fabricated using the following process (**Table S1**).

Table S1. Dry electrode fabrication processes.

Unit Process		Equipment	Input *	Time	Temp.	Process Parameters
Granule Formation	Mixing 1	Powder mill (LS-300, KMTech)	A + C	9 min	RT	12000/10 rpm
	Mixing 2	Powder mill (LS-300, KMTech)	(Mixing 1) + B	9 min	RT	12000/10 rpm
	Kneading	Kneader (NEP-0.5K, KMTech)	ABC composite (Mixing 2)	20 min	80 °C	10 rpm
	Grinding	Powder mill (LS-300, KMTech)	Electrode dough (Kneading)	20 s	RT	10000/10 rpm
Film Formation		Roll mill (KRM-80D, KMTech)	Electrode granule (Grinding)	1 time	80 °C	3 rpm, R/G 80 μm
Press		Roll press (MP-230H, Rohtec)	Electrode film (Film formation)	-	RT	5 mm s^{-1}, R/G 50-80 μm
Lamination		Roll press (MP-230H, Rohtec)	Electrode film + carbon-coated Al	1 time	RT	5 mm s^{-1}, R/G 80 μm
Vacuum Dry		Vacuum oven (OV-11, JeioTech)	Electrode	10 h	110 °C	Under vacuum

* A (active material), B (binder), C (conductive agent), R/G (roller gap)

Wet Electrode Fabrication

Wet-processed thick cathodes were fabricated in 10 g batches with a weight ratio of A/B/C = 97.0/1.5/1.5. In the coating process, slurry was coated onto the Al current collector (30 µm). The electrodes with an areal capacity of 10 mA h cm^{-2} were produced with a loading level of 45–50 mg cm^{-2} and a composite density range of 3.30 g cm^{-3}. Achieving high loading levels and composite densities through wet processes is challenging because of the drying process. Therefore, to minimize delamination between the composite and the current collector caused by binder non-uniformity during the drying process, the drying was carried at a low temperature of 40 °C. Wet electrodes were fabricated using the following process (**Table S2**).

Table S2. Wet electrode fabrication processes.

Unit Process	Equipment	Input *	Time	Temp.	Process Parameters
Mixing 1	Hand mix	A + C	15 min	RT	-
Mixing 2	Homogenizer (ED-1, Nissei)	B + NMP	15 min	RT	7000 rpm
Mixing 3	Homogenizer (ED-1, Nissei)	(Mixing 1) + (Mixing 2)	30 min	RT	5000 rpm, 5 min 10000 rpm, 25 min
Coating	Knife Coating Device (KP-3000V, Kipae E&T)	Slurry + Al (Mixing 3)	1 time	RT	20 mm s^{-1}
Drying	Convection Oven (OF-12GW, JeioTech)	Slurry-coated electrode (Coating)	3 h	40 °C	-
Press	Roll press (MP-230H, Rohtec)	Dried electrode	-	RT	5 mm s^{-1}, R/G 10-200 µm
Vacuum Dry	Vacuum oven (OV-11, JeioTech)	Electrode	10 h	110 °C	Under vacuum

* A (active material), B (binder), C (conductive agent), R/G (roller gap)

In Fig. 7(e) and Fig. S24–S27, artificial graphite (S350, BTR), carboxymethylcellulose (CMC, MAC350, Sunrose), and styrene-butadiene rubber (SBR, BM-451B, Zeon) were used as the active material and binders for the anode, respectively. Graphite anode was fabricated by the wet electrode process to 11 mA h cm^{-2} considering the N/P ratio 1.1 (33.0 mg cm^{-2}, 250 µm, and 1.45 g cm^{-3}), with a composition ratio of graphite/CMC/SBR = 97.4/1.2/1.4 by weight.

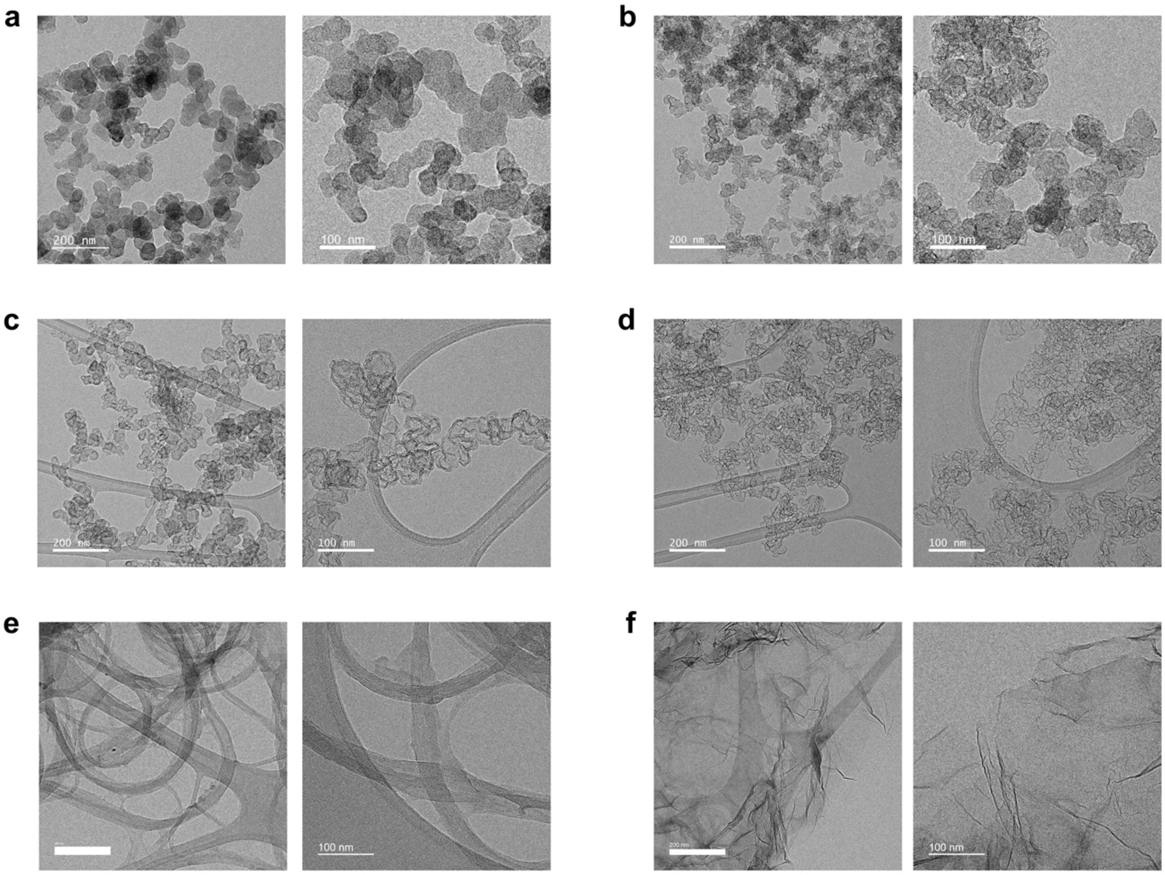

Fig. S1. Low-magnification TEM images of the conductive agents in Fig. 2(a). (a) SP (Super P). (b) DB (Li-435). (c) KB (EC-300J). (d) KB (EC-600JD). (e) CNT (Tuball). (f) Graphene (N002-PDR).

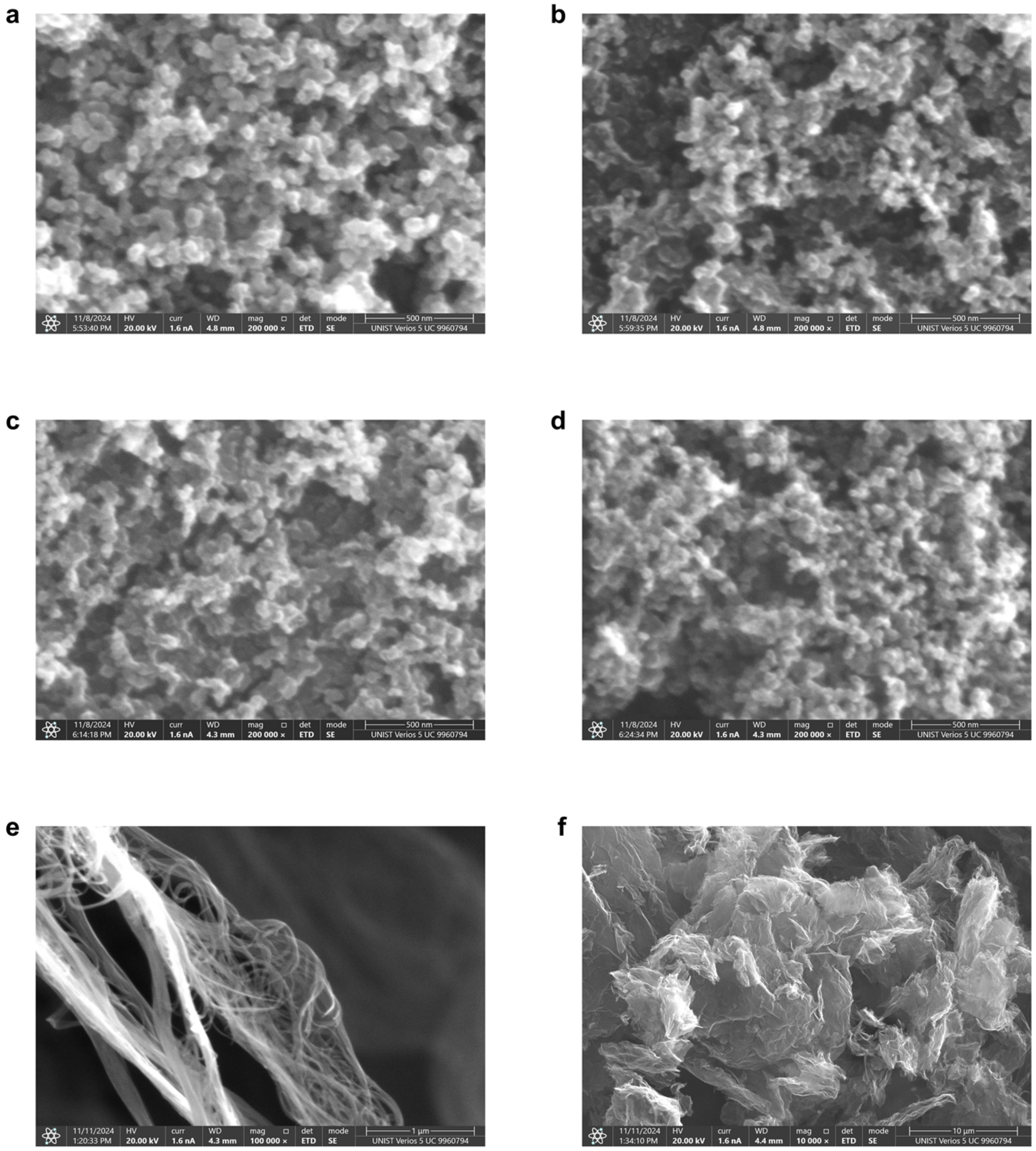

Fig. S2. SEM images of the conductive agents. (a) SP (Super P). (b) DB (Li-435). (c) KB (EC-300J). (d) KB (EC-600JD). (e) CNT (Tuball). (f) Graphene (N002-PDR). SEM images of CNT and graphene were selected with different magnifications for convenience.

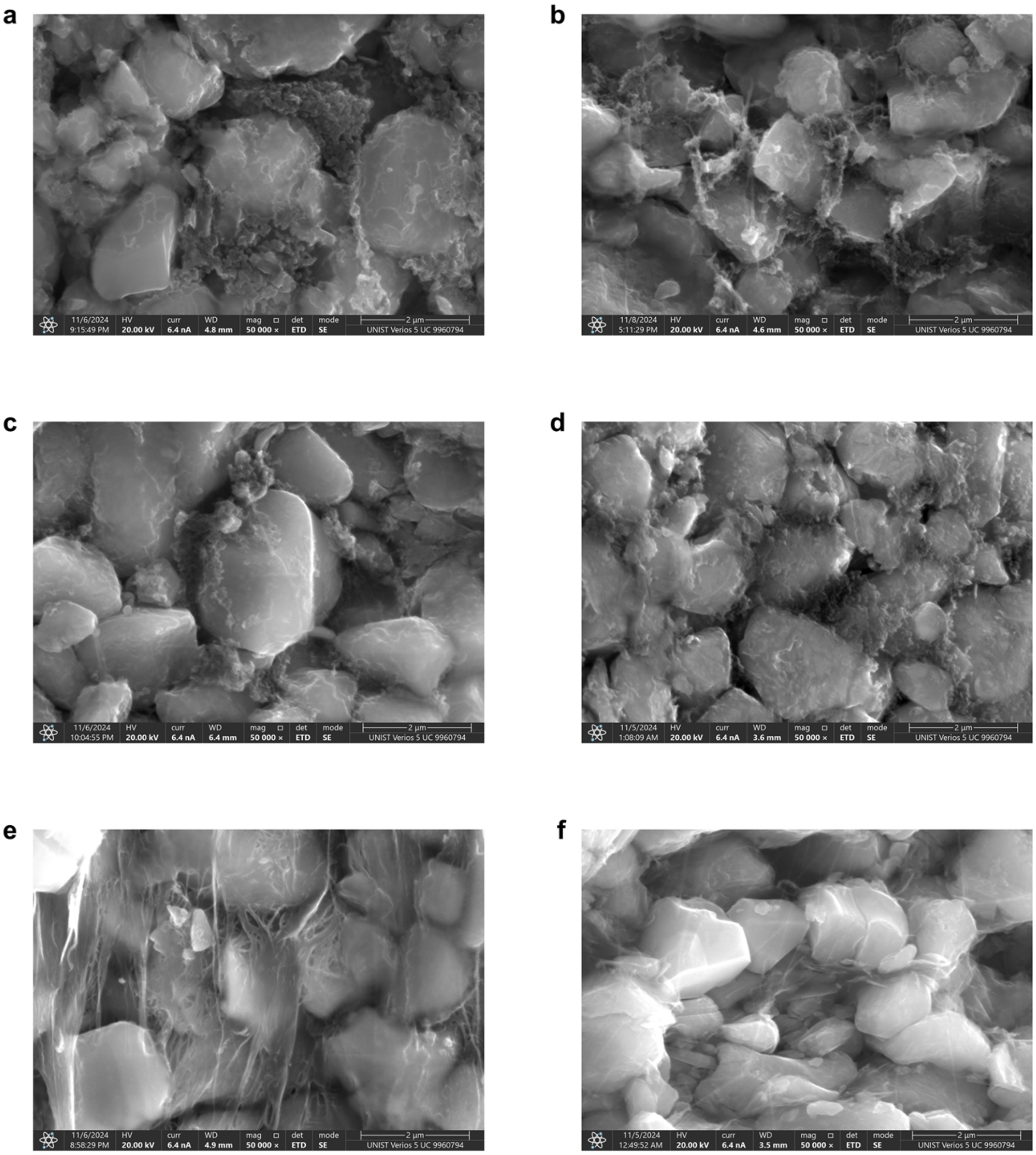

Fig. S3. SEM images of the cross-sectional (cut) electrodes by different conductive agents. (a) SP (Super P). (b) DB (Li-435). (c) KB (EC-300J). (d) KB (EC-600JD). (e) CNT (Tuball). (f) Graphene (N002-PDR).

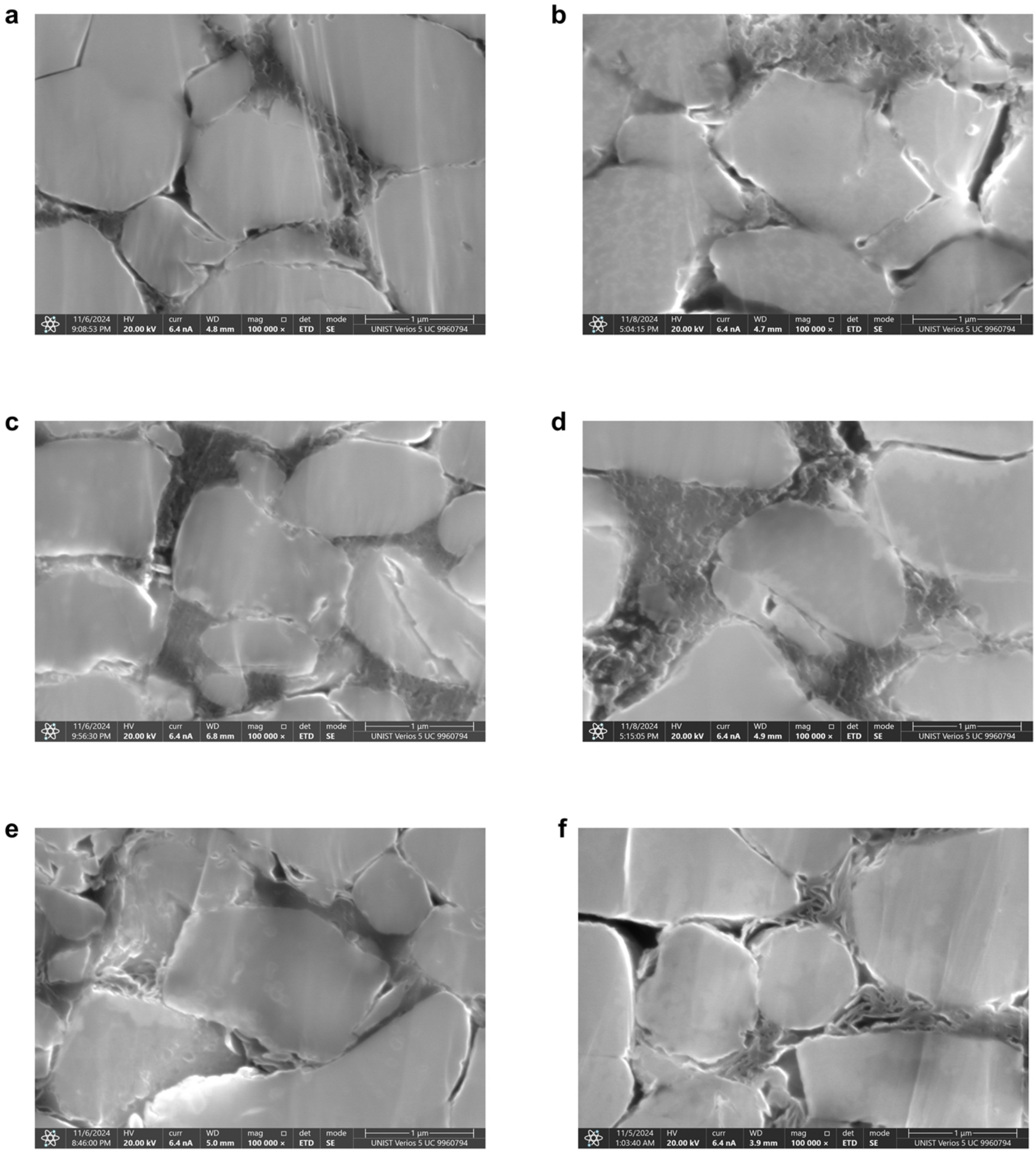

Fig. S4. SEM images of the cross-sectional (ion-milled) electrodes by different conductive agents. (a) SP (Super P). (b) DB (Li-435). (c) KB (EC-300J). (d) KB (EC-600JD). (e) CNT (Tuball). (f) Graphene (N002-PDR).

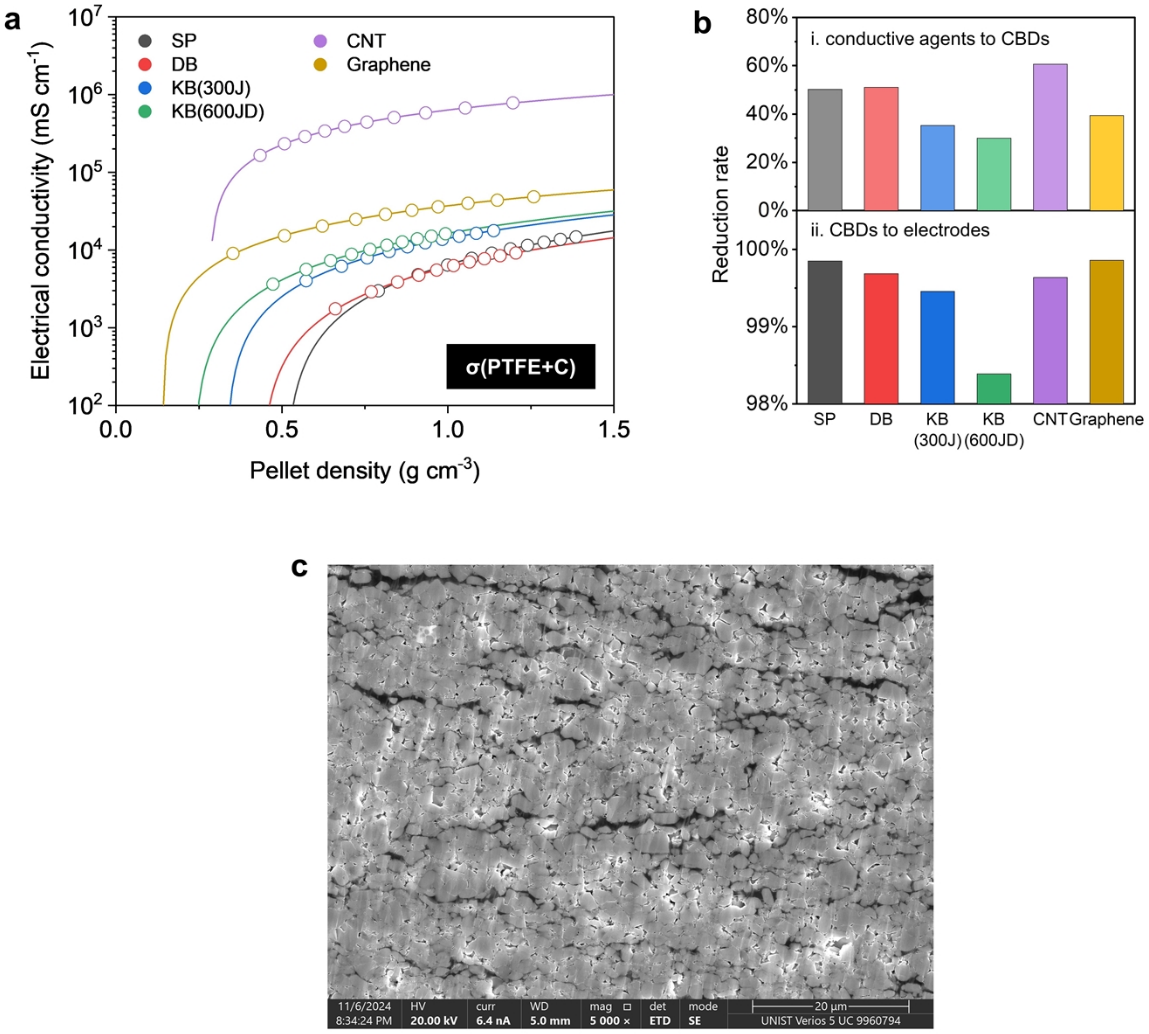

Fig. S5. (a) Electrical conductivities of carbon-binder composites (PTFE/conductive agent = 1/1) by powder resistivity measurement. (b) Reduction rate of electrical conductivity from conductive agents to carbon-binder composite (i), from carbon-binder composite to electrodes (ii) in Fig. 3(a). (c) Low magnification SEM image of the cathode with 2 wt% CNT.

Reduction rates of electrical conductivity were calculated using the equations below.

$$1 - \frac{\sigma(PTFE + C)}{\sigma(C)} \tag{i}$$

$$1 - \frac{\sigma(electrode)}{\sigma(PTFE + C)} \tag{ii}$$

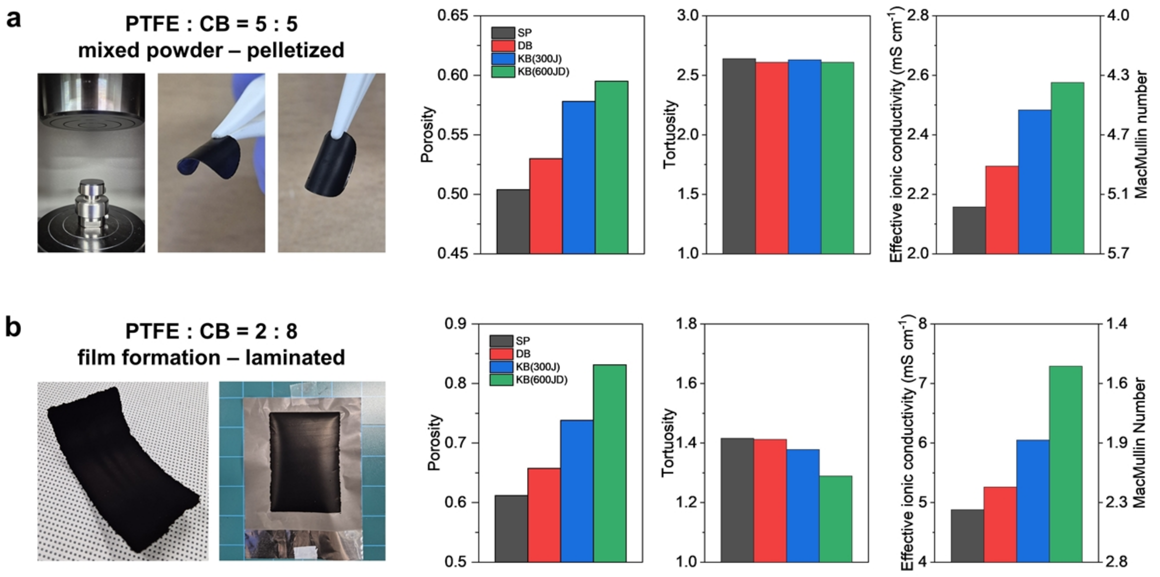

Fig. S6. CBD electrode fabrication and electrode parameter measurement. (a) PTFE/carbon black = 5/5, pelletized by 300 MPa. (b) PTFE/carbon black = 2/8, film formation – laminated.

Note that CNT and graphene conductive agents were excluded from the evaluation due to their morphological characteristics which are challenging to fabricate uniform CBD electrodes. By fabricating CBD electrodes without active material, the impact of the conductive agent itself on ionic conductivity can be indirectly assessed. The author analyzed the limitations of this experiment as follows:

1. The fabricated CBD electrodes do not precisely reflect the density and composition of CBD in actual electrodes.

2. In real electrodes, the microstructure is formed through mixing with active material, so the microstructure of CBD electrodes fabricated without active material cannot be assumed to match the CBD within actual electrodes.

Despite these limitations, relative comparisons among the four types of carbon black revealed that the effective ionic conductivity of KB(600JD) was approximately 20% higher than that of SP in (a) and around 50% higher in (b).

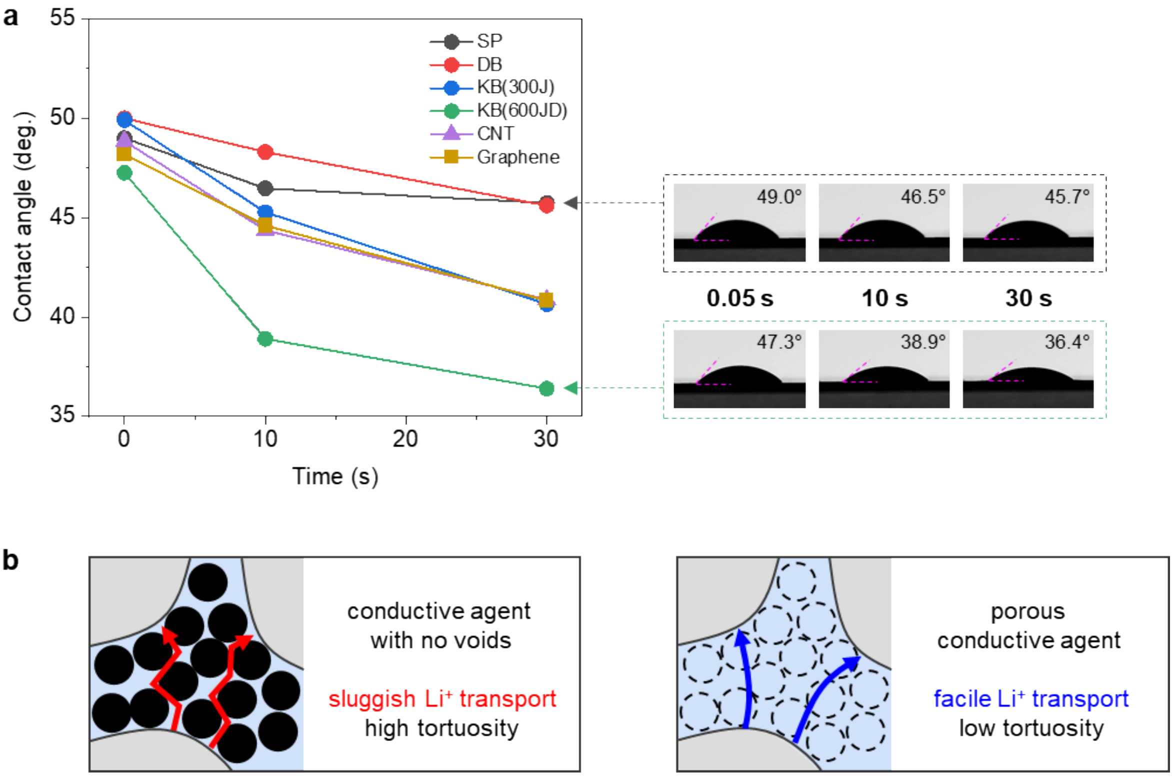

Fig. S7. (a) Contact angle measurement between dry-processed thick electrode and electrolyte. (b) Schematics of CBD with no voids in the conductive agents (left) and porous conductive agent (right).

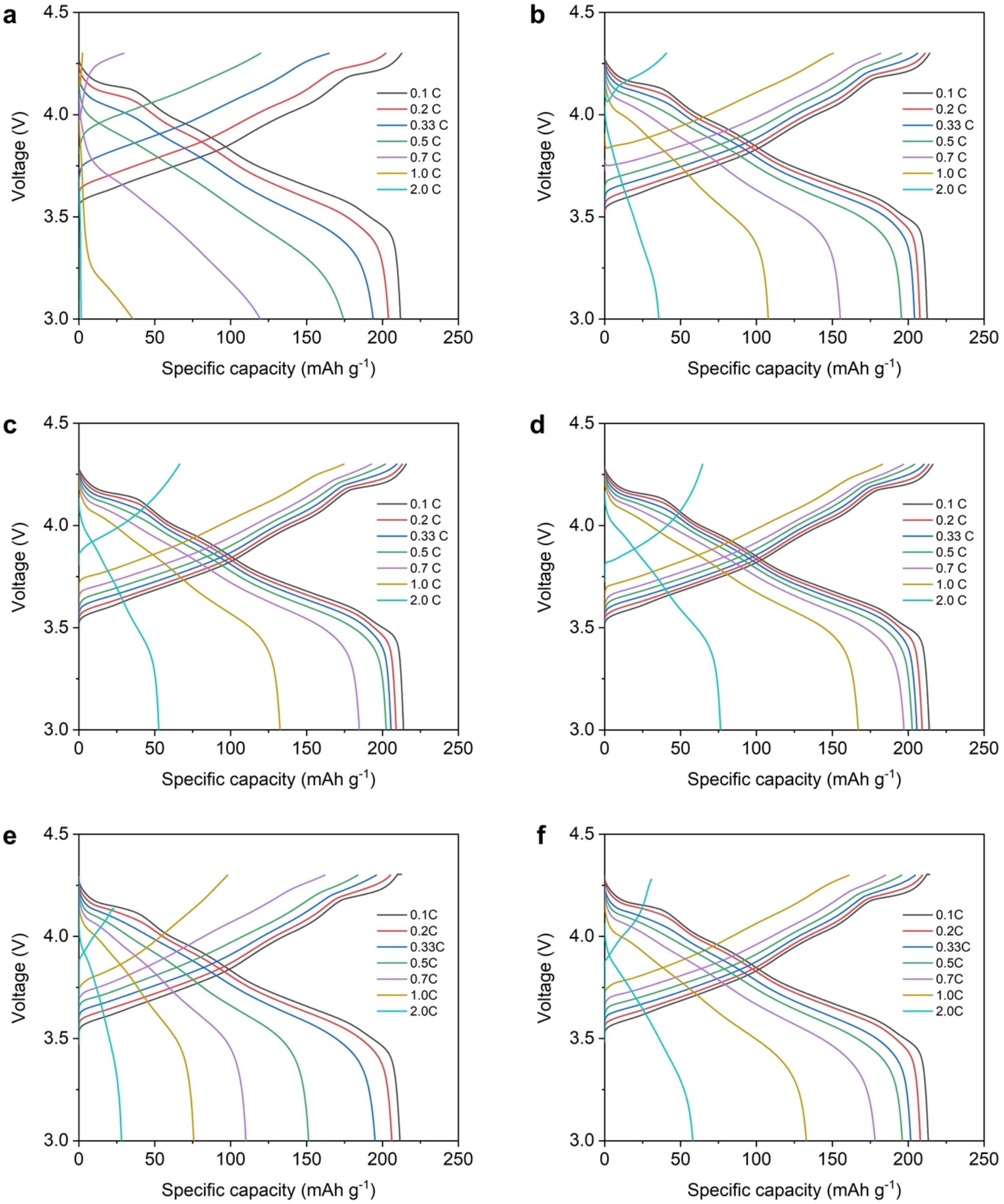

Fig. S8. Voltage profiles of rate capability test in Fig. 3(d). (a) SP (Super P). (b) DB (Li-435). (c) KB (EC-300J). (d) KB (EC-600JD). (e) CNT (Tuball). (f) Graphene (N002-PDR).

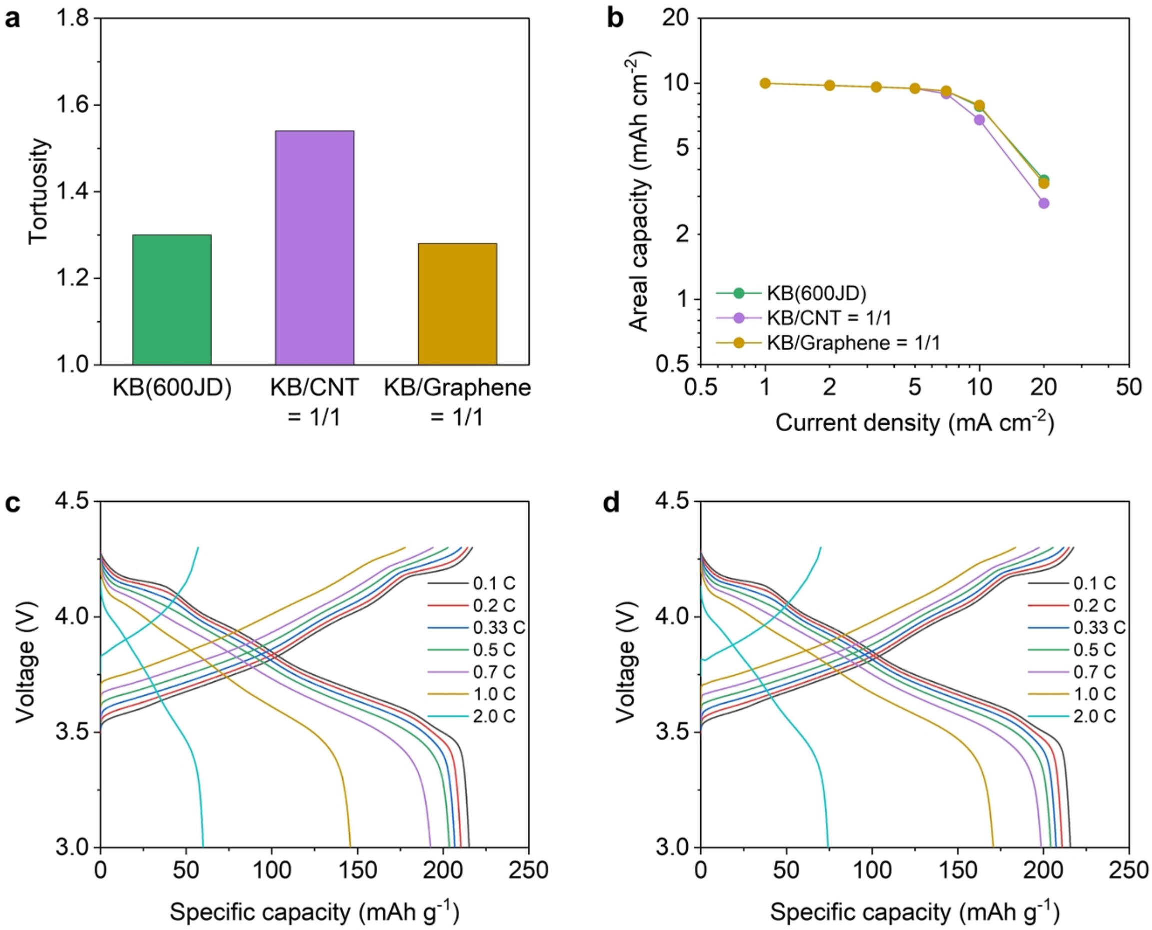

Fig. S9. Tortuosity measurement and electrochemical evaluation with mixed conductive agents. (a) Tortuosity. (b) Discharge rate capability. (c) KB/CNT = 1/1. (d) KB/Graphene = 1/1.

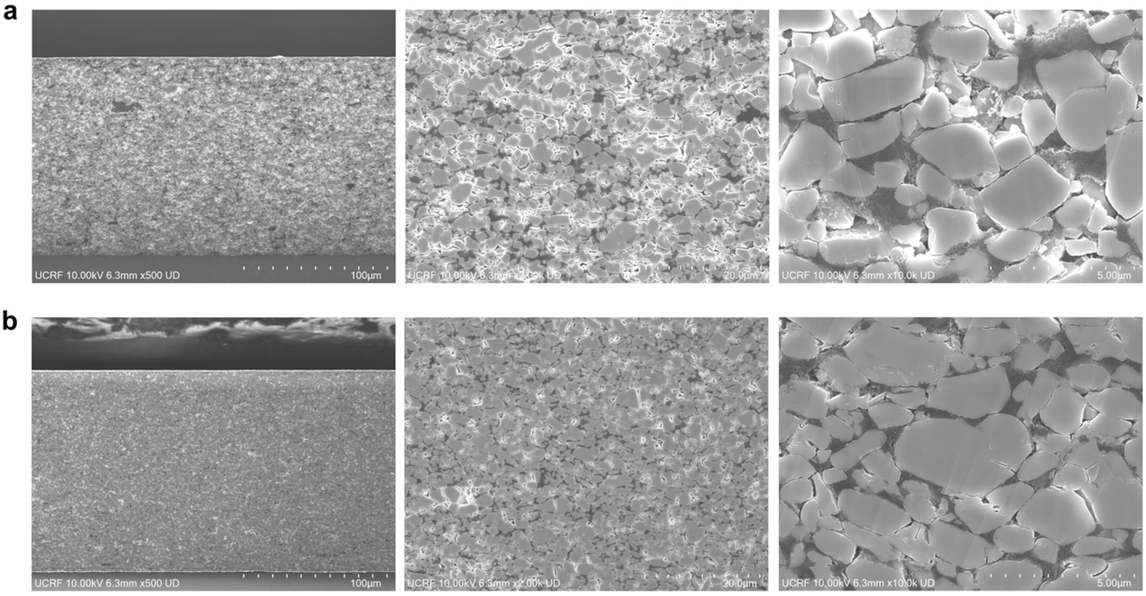

Fig. S10. Cross-sectional SEM images for different magnifications in Fig. 4(a). (a) Wet-processed electrode. (b) Dry-processed electrode.

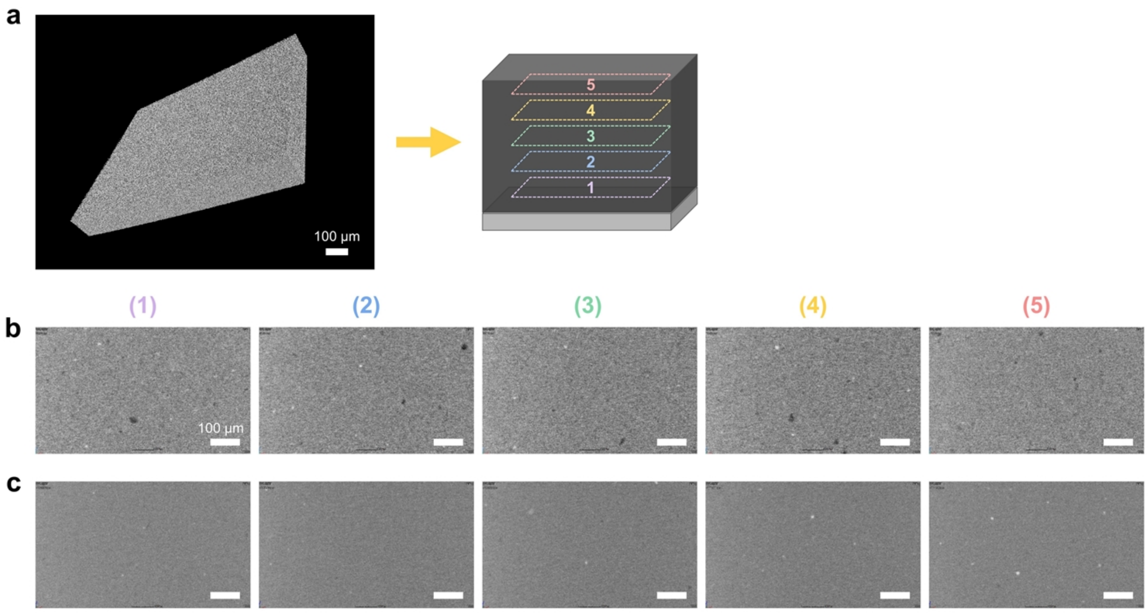

Fig. S11. X-ray CT analysis. (a) 3D reconstructed electrode and schematic of its observed region. (b) Wet-processed electrode. (c) Dry-processed electrode.

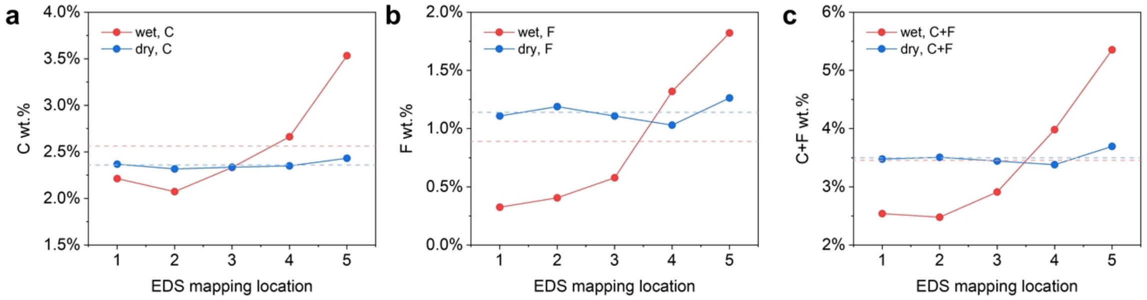

Fig. S12. EDS quantification results for different mapping locations in Fig. 4(a). Scan range of each mapping location was 260 μm × 32 μm. (a) C distribution. (b) F distribution. (c) C+F distribution.

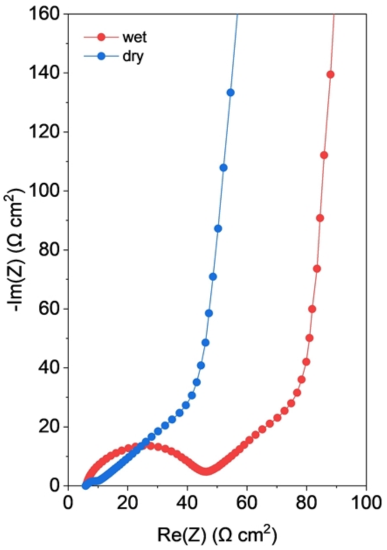

	● wet	● dry
Composite density [g cm^{-3}]	3.30	3.65
Composite thickness [μm]	140	140
Ionic resistance [ohm]	69.1	65.3
Porosity	0.211	0.165
Tortuosity	1.8	1.3

Fig. S13. Symmetric cell EIS analysis for measuring tortuosity in Fig. 4(b). (a) Wet-processed electrode. (b) Dry-processed electrode.

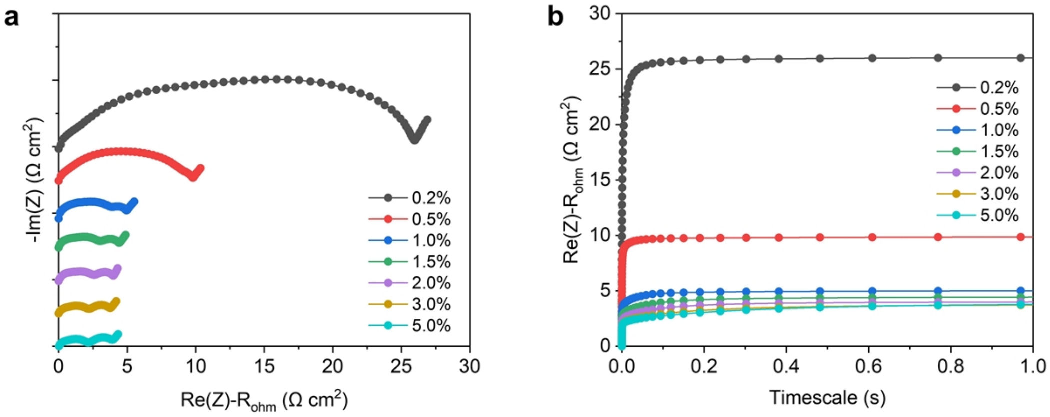

Fig. S14. Half-cell EIS analysis in Fig. 5(f). (a) Nyquist plot. (b) Internal resistance by time, where timescale indicates reciprocal value of frequency.

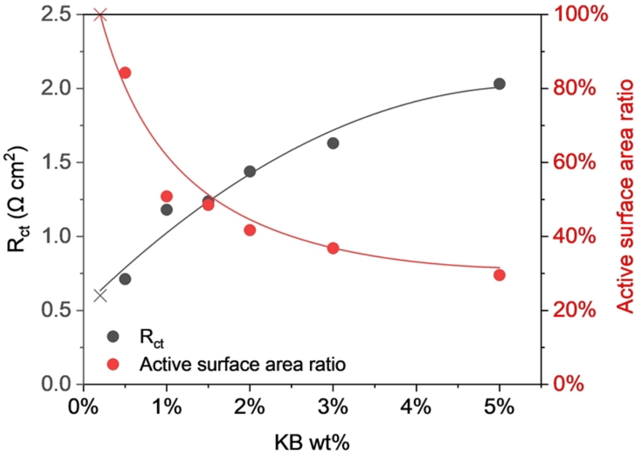

Fig. S15. Fitted results of charge transfer resistance (R_{ct}) in Fig. 5(f) and calculated active surface area ratio, assuming that active surface area ratio of KB 0.2 wt% was 100%.

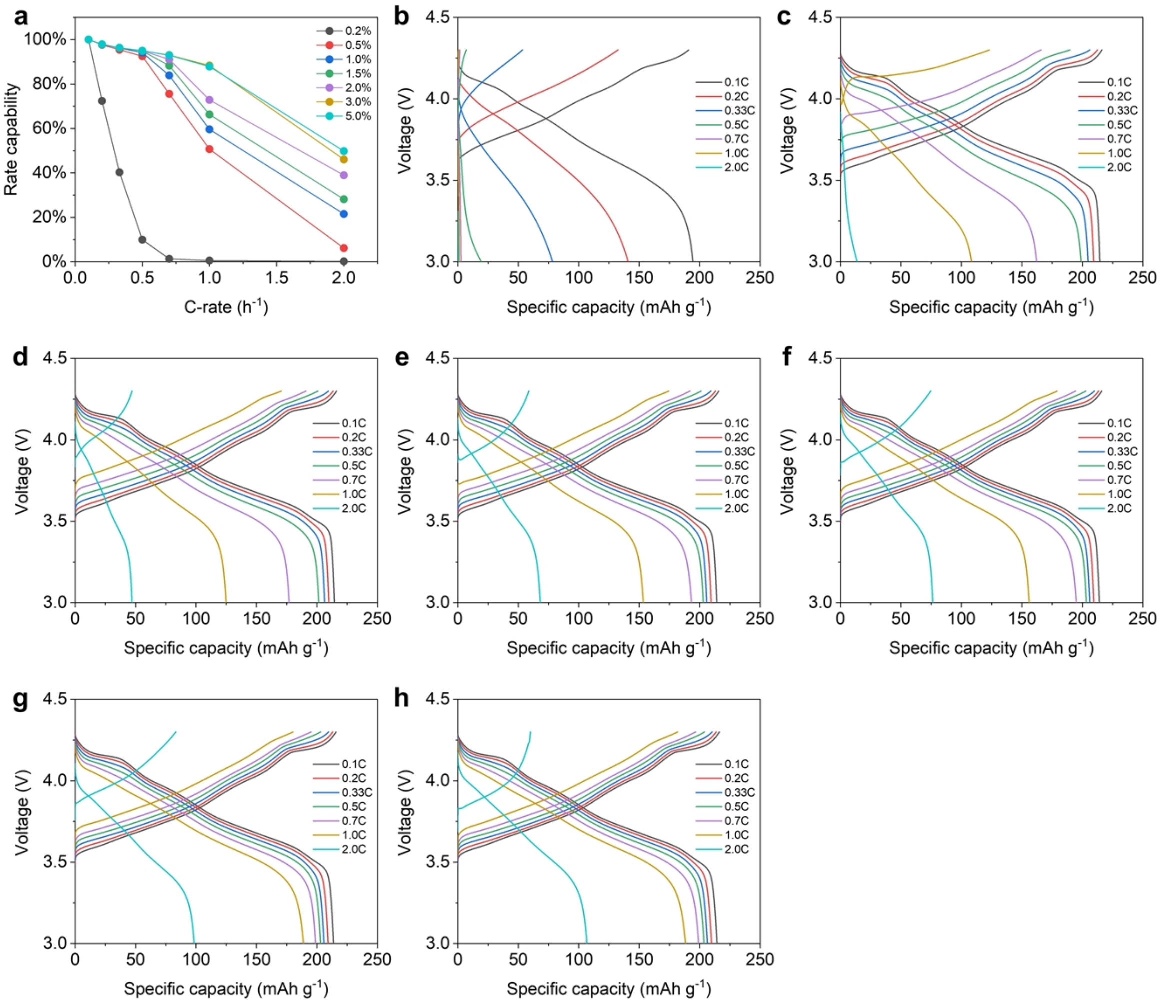

Fig. S16. Voltage profiles of rate capability test by content of KB (EC-600JD) in Fig. 5(g). (a) Discharge rate capabilities by C-rate. (b) KB 0.2 wt%. (c) KB 0.5 wt%. (d) KB 1.0 wt%. (e) KB 1.5 wt%. (f) KB 2.0 wt%. (g) KB 3.0 wt%. (h) KB 5.0 wt%.

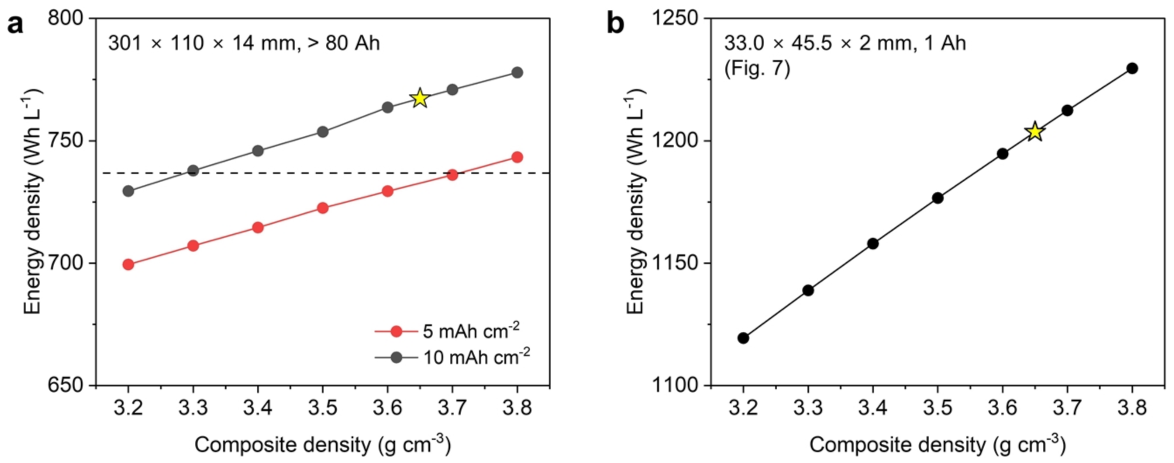

Fig. S17. Energy density calculated by the composite density of cathodes. Yellow stars indicate this study (KB 2.0 wt%). (a) Commercial NCM811/Gr pouch full cell (N/P 1.05, 1.5 g cm^{-3}, 345 mA h g^{-1} graphite anode). (b) 1 A h NCM811/Li pouch cell in Fig. 7.

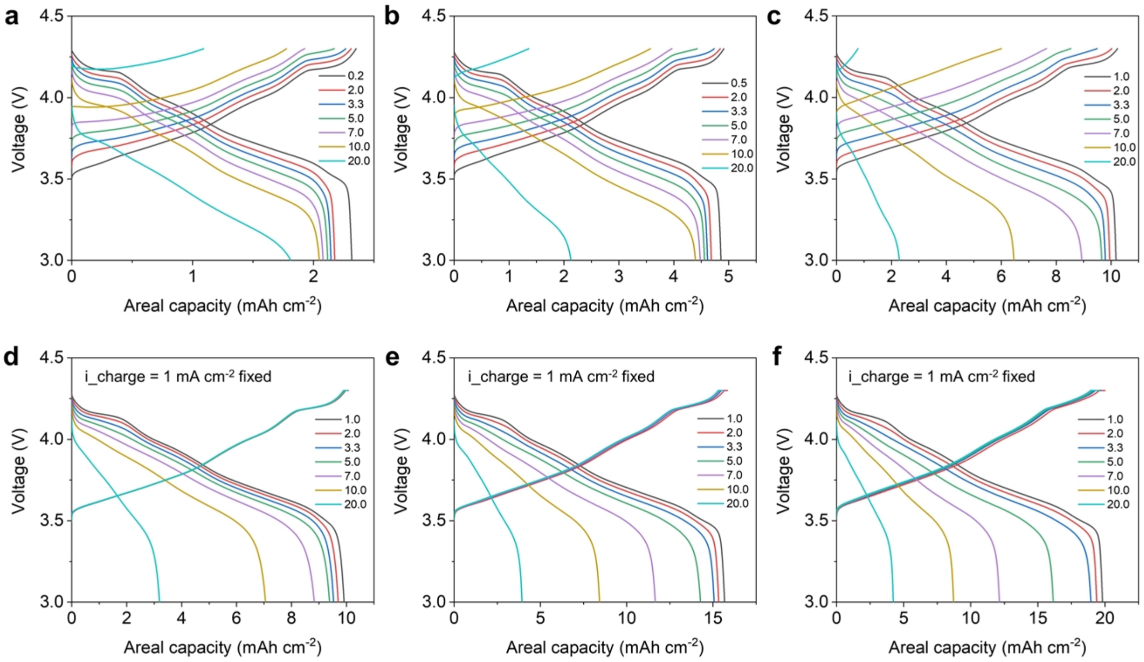

Fig. S18. Voltage profiles of rate capability test in Fig. 6(c). Numbers in legends indicate applied current density (mA cm^{-2}). (a) Wet, 2 mA h cm^{-2}. (b) Wet, 5 mA h cm^{-2}. (c) Wet, 10 mA h cm^{-2}. (d) Dry, 10 mA h cm^{-2}. (e) Dry, 15 mA h cm^{-2}. (f) Dry, 20 mA h cm^{-2}.

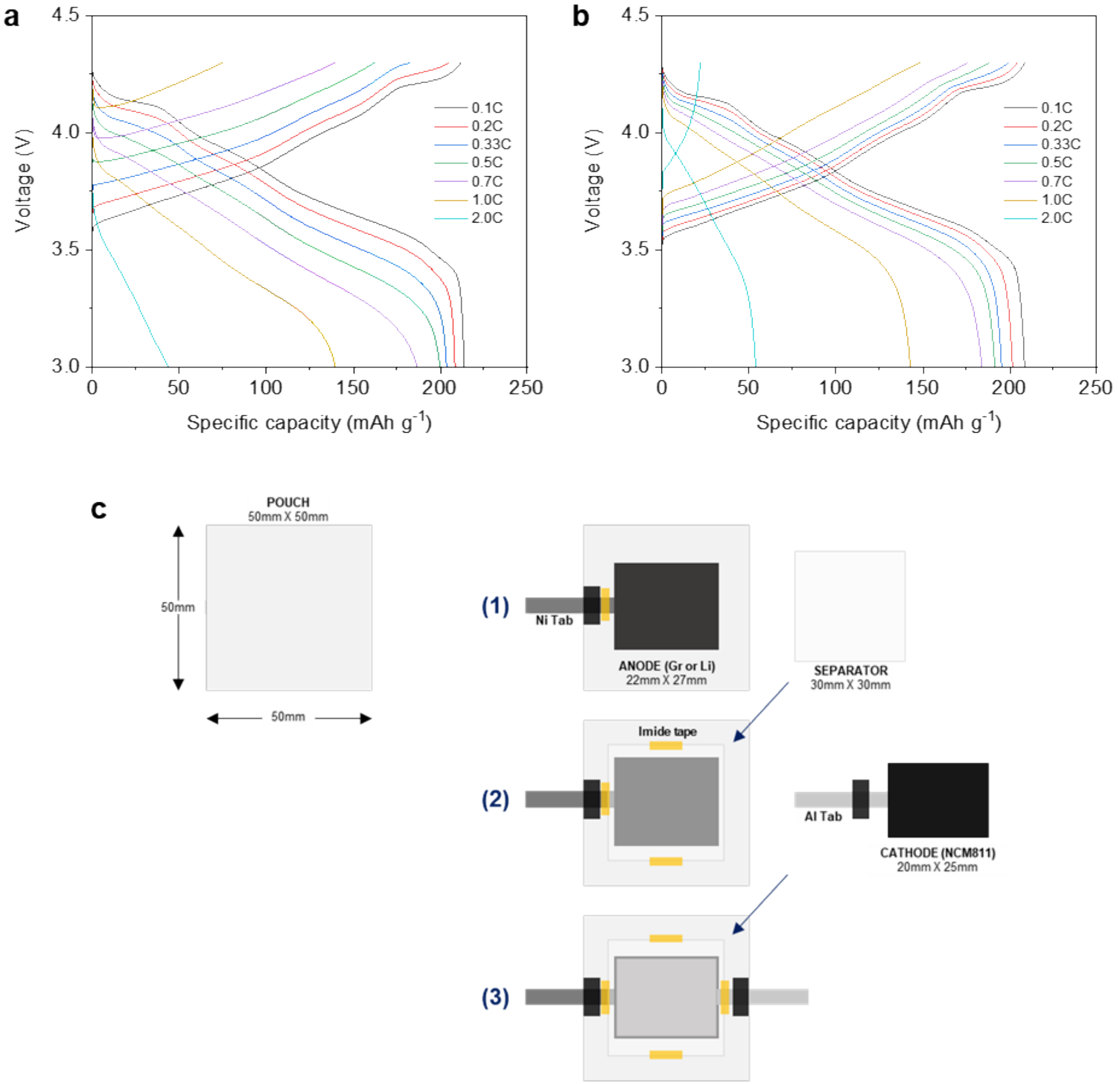

Fig. S19. Voltage profiles of rate capability test in comparison with electrode fabrication method by single-sided pouch cell configuration. (a) single-sided pouch cell, wet-processed, (b) single-sided pouch cell, dry-processed. (c) Fabrication process of single-sided pouch cell.

10 mA h cm^{-2} cathodes and 100 μm Li metal were used to assemble single-sided pouch cell (N/P ratio = 2, E/C ratio = 2 g Ah^{-1}).

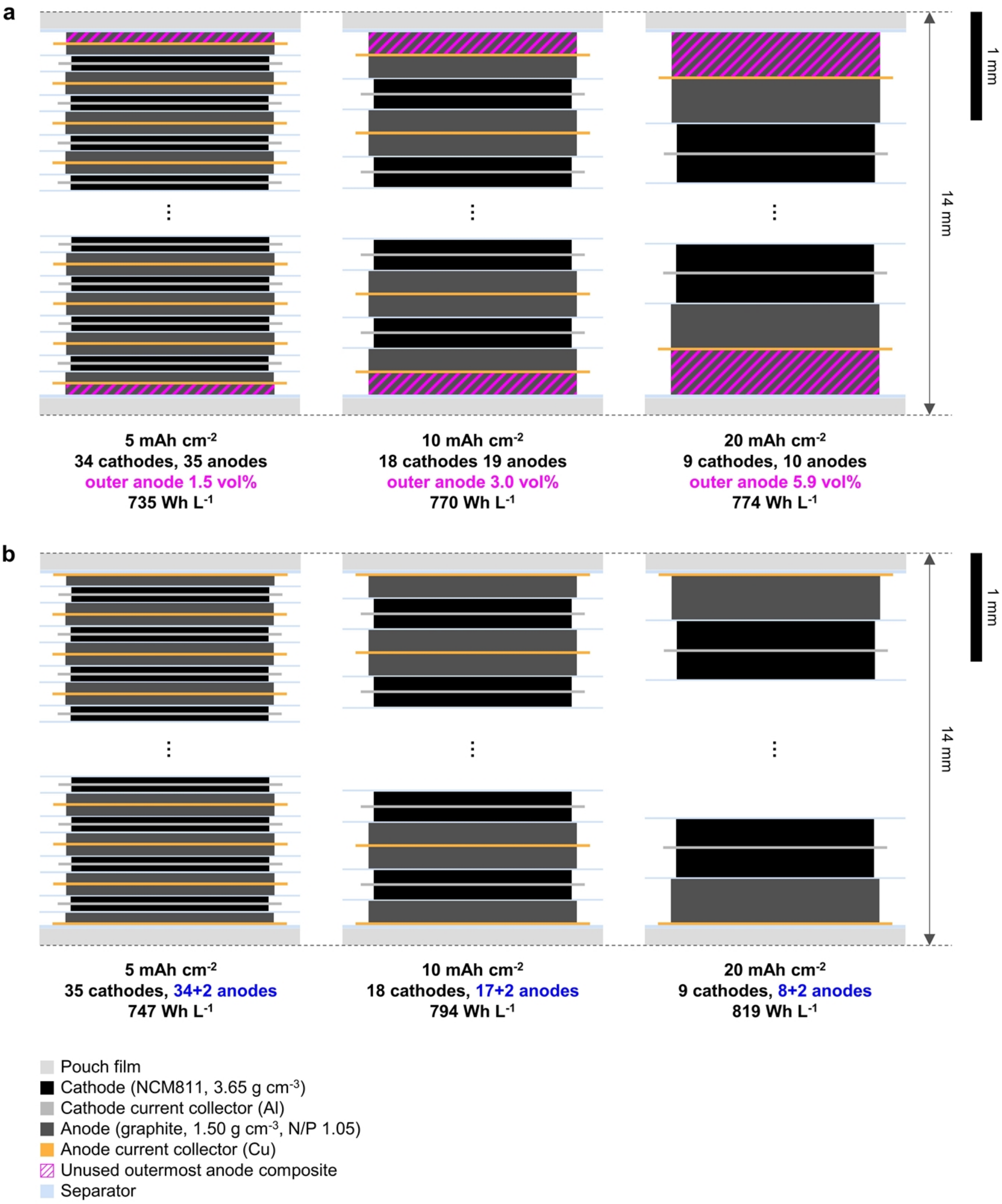

Fig. S20. Schematic illustrating impact of increased areal capacity on the energy density of the cell, highlighting the effect of the unused anode composite at outermost layers in Fig. 6(e). (a) Conventional design for pouch cell. (b) Design with single-sided anodes at outermost part.

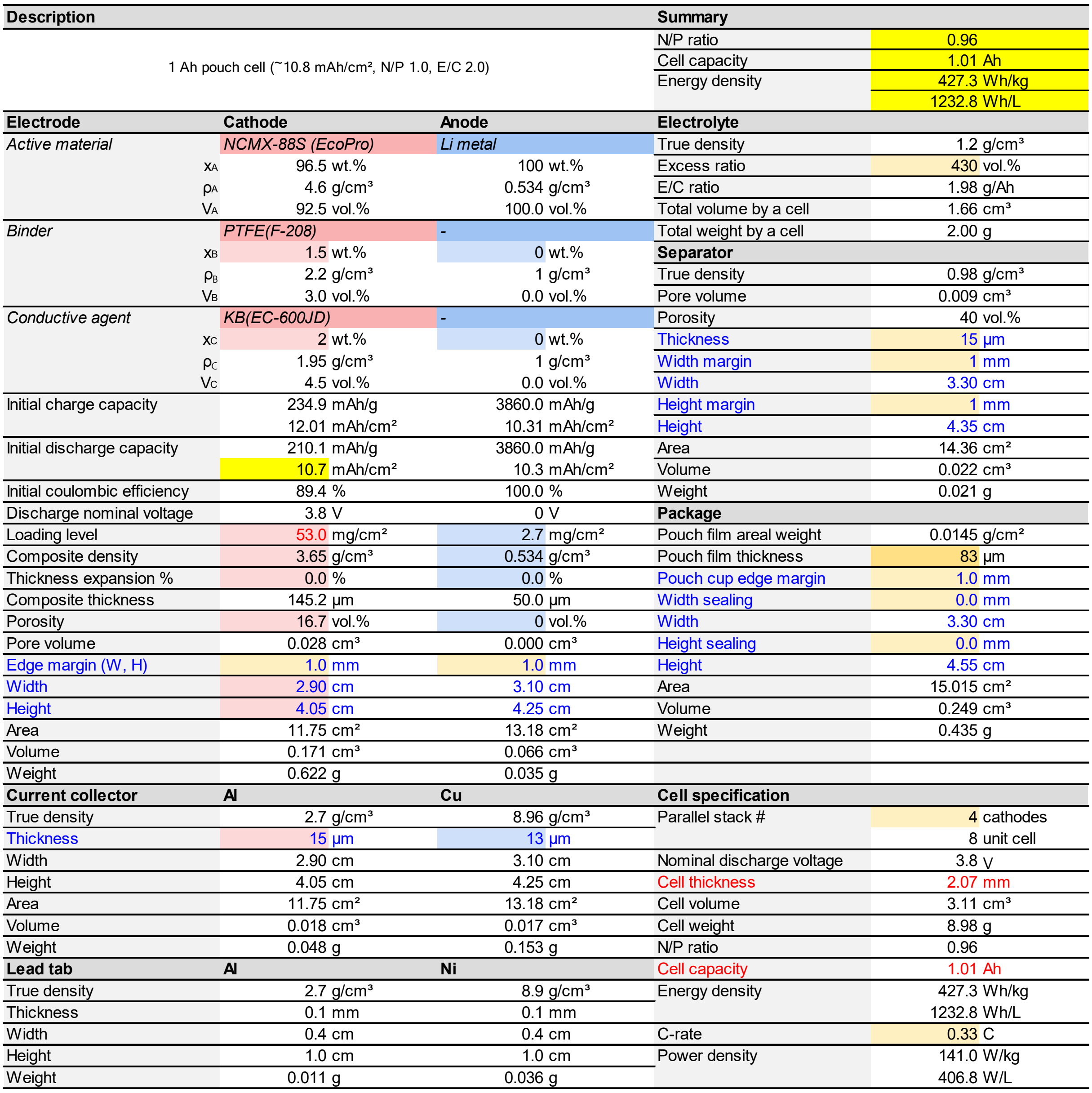

Description				**Summary**	
1 Ah pouch cell (~10.8 mAh/cm², N/P 1.0, E/C 2.0)				N/P ratio	0.96
				Cell capacity	1.01 Ah
				Energy density	427.3 Wh/kg
					1232.8 Wh/L
Electrode		**Cathode**	**Anode**	**Electrolyte**	
Active material		*NCMX-88S (EcoPro)*	*Li metal*	True density	1.2 g/cm³
	x_A	96.5 wt.%	100 wt.%	Excess ratio	430 vol.%
	ρ_A	4.6 g/cm³	0.534 g/cm³	E/C ratio	1.98 g/Ah
	V_A	92.5 vol.%	100.0 vol.%	Total volume by a cell	1.66 cm³
Binder		*PTFE(F-208)*	-	Total weight by a cell	2.00 g
	x_B	1.5 wt.%	0 wt.%	**Separator**	
	ρ_B	2.2 g/cm³	1 g/cm³	True density	0.98 g/cm³
	V_B	3.0 vol.%	0.0 vol.%	Pore volume	0.009 cm³
Conductive agent		*KB(EC-600JD)*	-	Porosity	40 vol.%
	x_C	2 wt.%	0 wt.%	Thickness	15 µm
	ρ_C	1.95 g/cm³	1 g/cm³	Width margin	1 mm
	V_C	4.5 vol.%	0.0 vol.%	Width	3.30 cm
Initial charge capacity		234.9 mAh/g	3860.0 mAh/g	Height margin	1 mm
		12.01 mAh/cm²	10.31 mAh/cm²	Height	4.35 cm
Initial discharge capacity		210.1 mAh/g	3860.0 mAh/g	Area	14.36 cm²
		10.7 mAh/cm²	10.3 mAh/cm²	Volume	0.022 cm³
Initial coulombic efficiency		89.4 %	100.0 %	Weight	0.021 g
Discharge nominal voltage		3.8 V	0 V	**Package**	
Loading level		53.0 mg/cm²	2.7 mg/cm²	Pouch film areal weight	0.0145 g/cm²
Composite density		3.65 g/cm³	0.534 g/cm³	Pouch film thickness	83 µm
Thickness expansion %		0.0 %	0.0 %	Pouch cup edge margin	1.0 mm
Composite thickness		145.2 µm	50.0 µm	Width sealing	0.0 mm
Porosity		16.7 vol.%	0 vol.%	Width	3.30 cm
Pore volume		0.028 cm³	0.000 cm³	Height sealing	0.0 mm
Edge margin (W, H)		1.0 mm	1.0 mm	Height	4.55 cm
Width		2.90 cm	3.10 cm	Area	15.015 cm²
Height		4.05 cm	4.25 cm	Volume	0.249 cm³
Area		11.75 cm²	13.18 cm²	Weight	0.435 g
Volume		0.171 cm³	0.066 cm³		
Weight		0.622 g	0.035 g		
Current collector		**Al**	**Cu**	**Cell specification**	
True density		2.7 g/cm³	8.96 g/cm³	Parallel stack #	4 cathodes
Thickness		15 µm	13 µm		8 unit cell
Width		2.90 cm	3.10 cm	Nominal discharge voltage	3.8 V
Height		4.05 cm	4.25 cm	Cell thickness	2.07 mm
Area		11.75 cm²	13.18 cm²	Cell volume	3.11 cm³
Volume		0.018 cm³	0.017 cm³	Cell weight	8.98 g
Weight		0.048 g	0.153 g	N/P ratio	0.96
Lead tab		**Al**	**Ni**	Cell capacity	1.01 Ah
True density		2.7 g/cm³	8.9 g/cm³	Energy density	427.3 Wh/kg
Thickness		0.1 mm	0.1 mm		1232.8 Wh/L
Width		0.4 cm	0.4 cm	C-rate	0.33 C
Height		1.0 cm	1.0 cm	Power density	141.0 W/kg
Weight		0.011 g	0.036 g		406.8 W/L

Fig. S21. 1 A h pouch cell design and energy density calculation in Fig. 7.

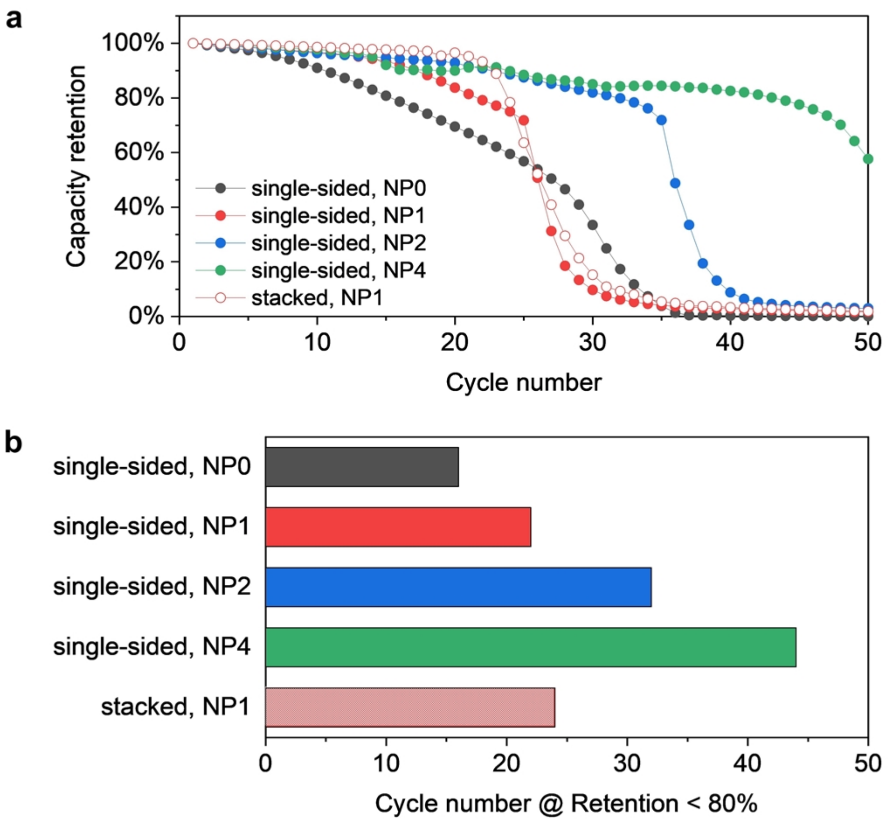

Fig. S22. Cycle life evaluation of single-sided pouch cell by N/P ratio by adjusting the thickness of Li metal anode. (a) Capacity retention. (b) The cycle number at which the capacity retention first drops below 80%.

10 mA h cm^{-2} cathodes and 0, 50, 100, 200 μm Li metal were used to assemble single-sided pouch cell (N/P ratio = 0, 1, 2, 4, E/C ratio = 2 g Ah^{-1}).

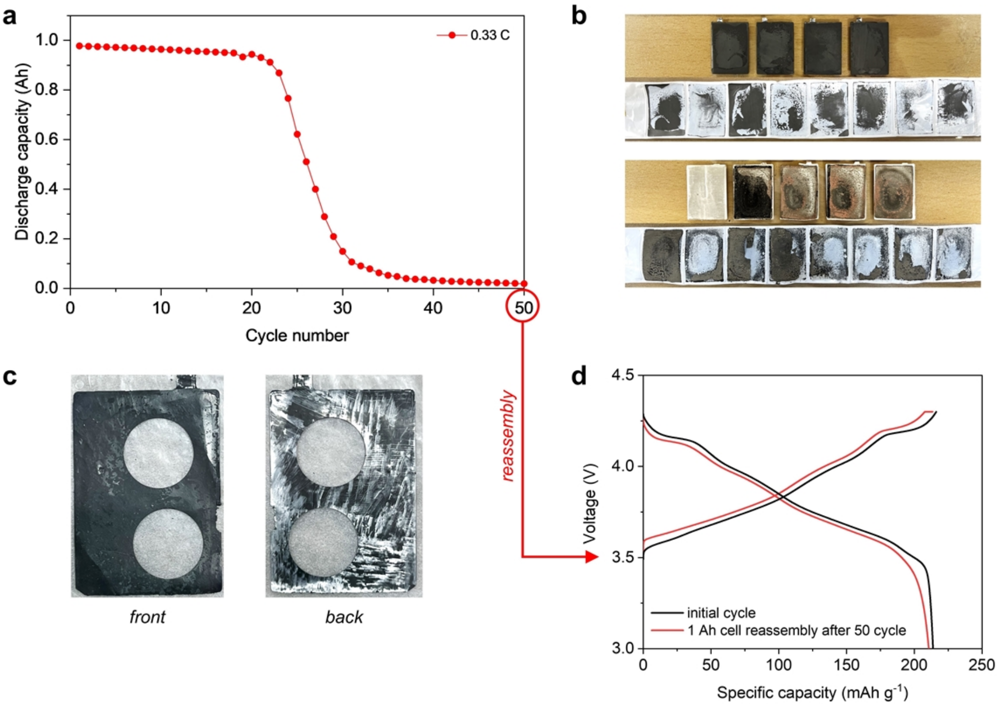

Fig. S23. Post-mortem analysis of cycled 1 A h pouch cell in Fig. 7(d). (a) Cycle life testing at 0.33 C. (b) Photographs of NCM cathode (top) and Li metal anode (bottom), along with both sides of separator after 50 cycles. (c) Extracted cathode was punched and reassembled into coin half-cells, with one side of double-sided cathode mechanically peeled off using a sharp knife. (d) Comparison of voltage profile between initial cycle and that for reassembled coin half-cell after 50 cycles.

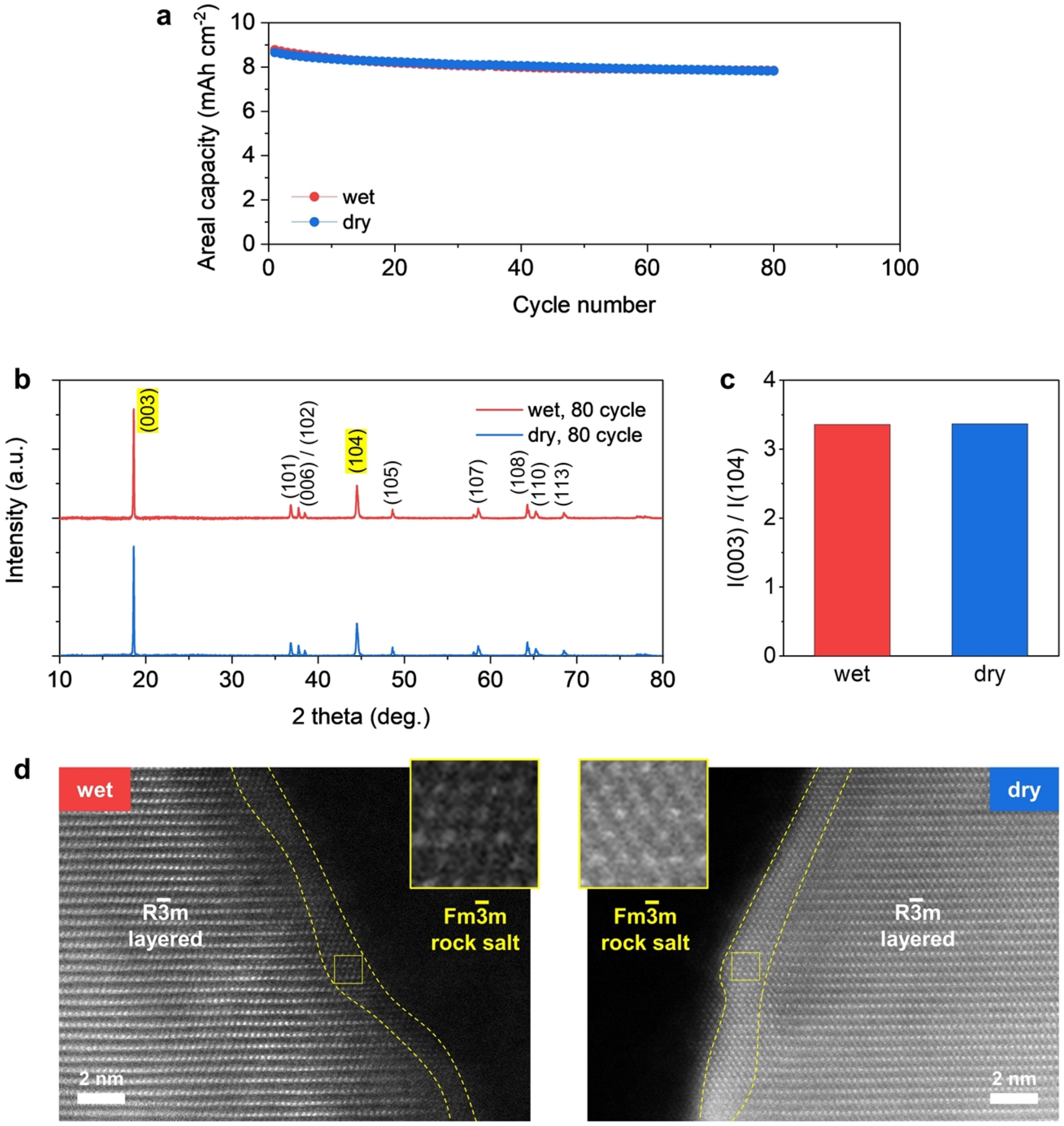

Fig. S24. Structural degradation analysis of electrodes after cycle life evaluation. (a) Cycle life characteristics of the single-sided pouch full cell at 0.33 C. (b) Structural degradation analysis through XRD after 80 cycles. (c) Intensity ratio of XRD, I(003) / I(104). (d) HAADF-STEM images of the cycled NCM particle from the wet-processed electrode (left) and the dry=processed electrode (right) after 80 cycles. Phase transition of about 2 nm thickness from rock salt to layered was observed owing to the cation mixing.

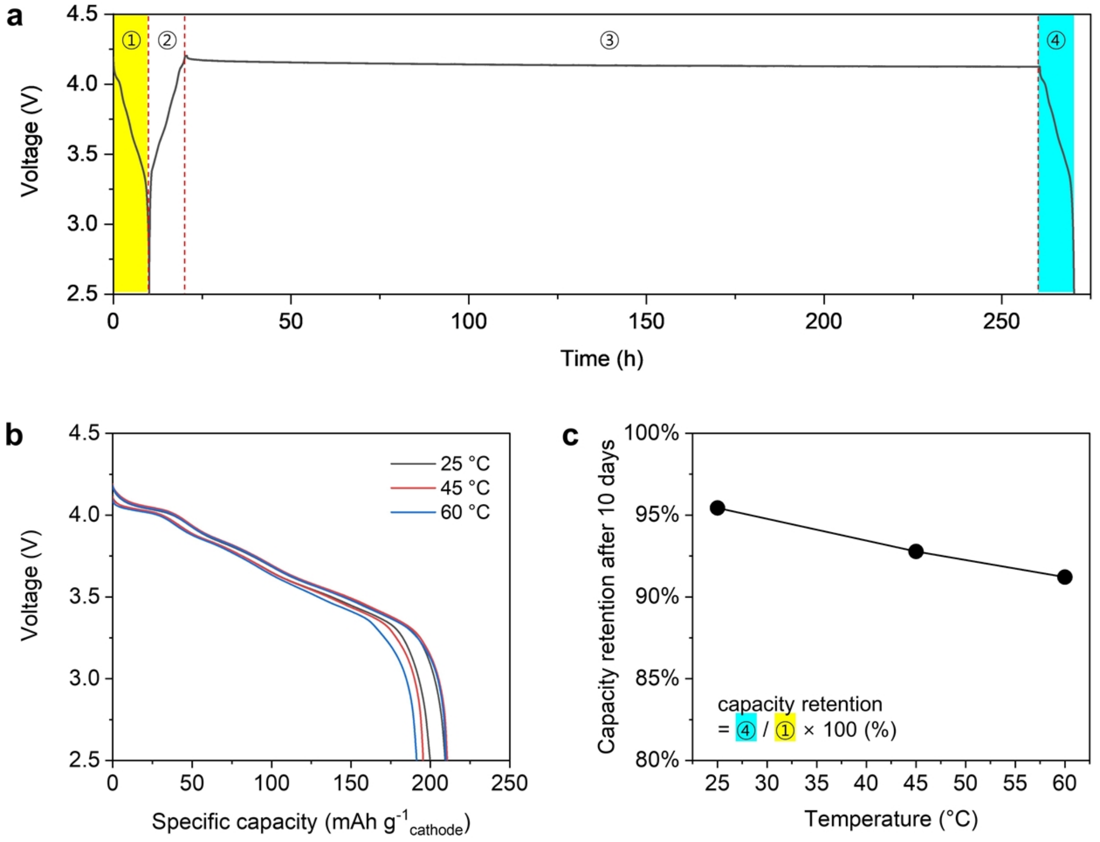

Fig. S25. Full cell storage test under different temperatures. (a) Long-term storage evaluation protocol: ① 0.1 C discharge – ② 0.1 C charge – ③ 10-day storage – ④ 0.1 C discharge. All charging, discharging, and storage steps were performed under specified temperature conditions. (b) Discharge voltage profiles from cycles ① and ④. (c) Capacity retention after 10 days.

During the 10-day storage test at varying temperatures, self-discharge rates of 5–10% were observed depending on the temperature. However, no significant capacity degradation was observed, even under high-temperature conditions.

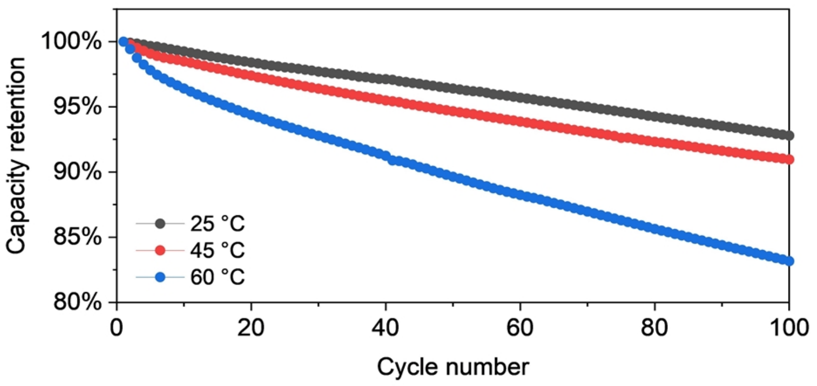

Fig. S26. Cycling performance of NCM811/graphite coin full cells at different temperatures.

No sudden drops in discharge capacities were investigated until 100 cycles, even under high-temperature conditions.

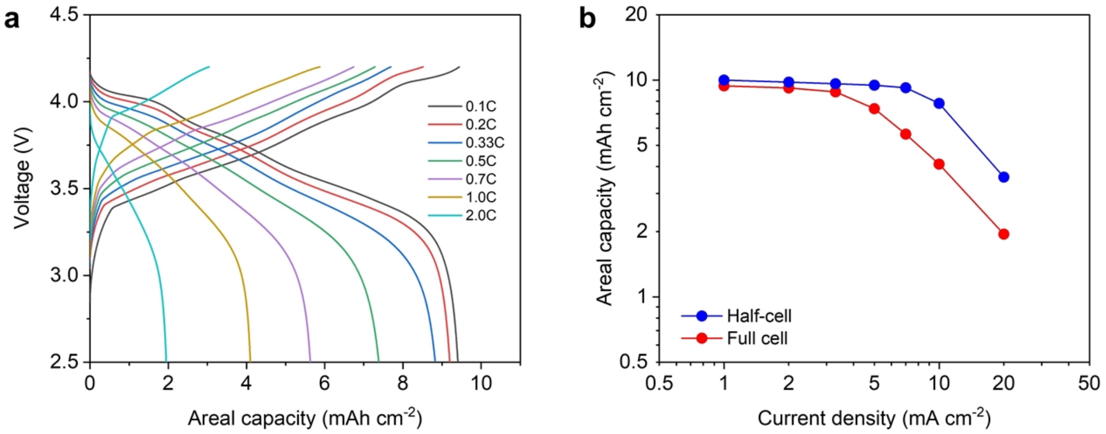

Fig. S27. (a) Voltage profile of full cell rate capability test. (b) Discharge rate capability of the half-cell and the full cell.

When conducting rate capability evaluations for full cells using a thick graphite anode, severe capacity degradation occurs above 0.33 C due to the high tortuosity of the graphite electrode. The graphite anode used in this study has a tortuosity of 6.5, which is significantly higher than the tortuosity of the dry-processed cathode with the porous spherical conductive agent, about 1.3. This difference in tortuosity results in rate capability limitations in full cells, primarily due to the characteristics of the graphite anode.

Table S3. Comparison of electrochemical performance between this study and previously reported dry-processed electrodes or wet-processed thick electrodes in Fig. 7(f).

Ref.		Methods	Active materials	Binders	Conductive agents	A	B	C	Loading level [mg cm^{-2}]	Thickness [μm]	Areal capacity [mA h cm^{-2}]	Composite density [g cm^{-3}]	Rate capability	Cycle number	Retention after cycles	Cycle conditions
*	dry	fibrillation	NCM811	PTFE	CB	96.5	1.5	2.0	51	140	10.6	3.64	73% @1C	418	80%	0.33C/0.33C
*	dry	fibrillation	NCM811	PTFE	CB	95.5	1.5	3.0	51	140	10.6	3.64	88% @1C	-	-	-
*	dry	fibrillation	NCM811	PTFE	CB	96.5	1.5	2.0	95	260	19.7	3.65	87% @0.25C	-	-	-
-	wet	commercial LIB	NCM811	PVDF	CB/CNT	96.0	2.0	2.0	~ 20	~ 57	~ 4	~ 3.5	-	-	-	-
S1	dry	fibrillation	NCM811	PTFE	CNT	85.0	5.0	10.0	71	209	12.1	3.40	86% @0.8C	100	75%	0.1C/0.1C
S2	dry	fibrillation	NCA/CNT	PTFE	-	99.6	0.4	-	40	100	8.0	4.00	85% @1C	120	80%	0.5C/0.5C
S3	dry	fibrillation	NCM622	PTFE	CB	92.0	5.0	3.0	35.5	115	5.5	3.09	89% @0.5C	300	79%	0.2C/0.2C
S4	dry	fibrillation	LNMO	PTFE	VGCF	93	2	5	22	90	3.0	2.44	-	300	80%	0.33C/0.33C
S5	dry	fibrillation	NCA	PTFE	CB/Graphene	96	2.2	1.8	50	140	10.0	3.57	90% @1C	100	82%	0.2C/0.5C
S6	dry	press	NCM712	PVDF	CNT	80.0	5.0	15.0	100	573	17.6	1.75	-	25	88%	0.1C/0.1C
S7	dry	press	NCM811	phenoxy resin	CNT	95.5	3.0	1.5	40	150	7.5	2.67	-	50	74%	0.1C/0.1C
S8	dry	spraying	NCM	PVDF	CB	90.0	5.0	5.0	63	200	9.1	3.15	58% @0.2C	3	80%	0.2C/0.2C
S9	wet	slurry casting	NCM622	PVDF	CB/Graphite	93.0	4.0	3.0	50	159	8.0	3.14	70% @0.75C	-	-	-
S10	wet	slurry casting	NCM111	PVDF	CB/Graphite	90.0	3.0	7.0	82	305	9.2	2.69	67% @ 0.33C	-	-	-
S11	wet	laser structuring	LCO	PVDF	CB	95.6	2.2	2.2	172	700	26.0	2.46	77% @0.05C	-	-	-
S12	wet	magnetic alignment	LCO	PVA	CB	95.0	2.5	2.5	100.5	440	13.8	2.28	74% @0.5C	-	-	-
S13	wet	wood structuring	LFP	epoxy	-	50.0	50.0	-	60	800	7.5	0.75	77% @ 0.27C	140	76%	0.27C/0.27C
S14	wet	meshed Al c.c.	NCM622	PVDF	CB/Graphite	92.0	4.0	4.0	44.2	200	7.6	2.21	63% @0.5C	-	-	-
S15	wet	meshed Al c.c.	NCM111	PVDF	CB	91.8	4.1	4.1	57.3	259	7.0	2.21	66% @0.5C	100	69%	0.2C/0.2C

* This work

References

S1. G. Park, H.-S. Kim and K. J. Lee, *Nanomaterials*, 2023, **13**, 324.

S2. J. Shin, J. H. Lee, J. K. Seo, W. T. A. Ran, S. M. Hwang and Y. J. Kim, *Int. J. Energy Res.*, 2022, **46**, 16061–16074.

S3. R. Tao, B. Steinhoff, X.-G. Sun, K. Sardo, B. Skelly, H. M. Meyer, C. Sawicki, G. Polizos, X. Lyu, Z. Du, J. Yang, K. Hong and J. Li, *Chem. Eng. J.*, 2023, **471**, 144300.

S4. W. Yao, M. Chouchane, W. Li, S. Bai, Z. Liu, L. Li, A. X. Chen, B. SayA hpour, R. Shimizu, G. Raghavendran, M. A. Schroeder, Y.-T. Chen, D. H. S. Tan, B. Sreenarayanan, C. K. Waters, A. Sichler, B. Gould, D. J. Kountz, D. J. Lipomi, M. Zhang and Y. S. Meng, *Energy Environ. Sci.*, 2023, **16**, 1620–1630.

S5. J. Kim, K. Park, M. Kim, H. Lee, J. Choi, H. B. Park, H. Kim, J. Jang, Y.-H. Kim, T. Song and U. Paik, *Adv. Energy Mater.*, 2024, **14**, 2303455.

S6. M. Ryu, Y.-K. Hong, S.-Y. Lee and J. H. Park, *Nat. Commun.*, 2023, **14**, 1316.

S7. H.-M. Kim, B.-I. Yoo, J.-W. Yi, M.-J. Choi and J.-K. Yoo, *Nanomaterials*, 2022, **12**, 3320.

S8. J. Liu, B. Ludwig, Y. Liu, Z. Zheng, F. Wang, M. Tang, J. Wang, J. Wang, H. Pan and Y. Wang, *Adv. Mater. Technol.*, 2017, **2**, 1700106.

S9. L. S. Kremer, A. Hoffmann, T. Danner, S. Hein, B. Prifling, D. Westhoff, C. Dreer, A. Latz, V. Schmidt and M. WohlfAhrt-Mehrens, *Energy Technol.*, 2020, **8**, 1900167.

S10. M. Singh, J. Kaiser and H. Hahn, *J. Electroanal. Chem.*, 2016, **782**, 245–249.

S11. J. Park, C. Jeon, W. Kim, S.-J. Bong, S. Jeong and H.-J. Kim, *J. Power Sources*, 2021, **482**, 228948.

S12. L. Li, R. M. Erb, J. Wang, J. Wang and Y.-M. Chiang, *Adv. Energy Mater.*, 2019, **9**, 1802472.

S13. C. Chen, Y. Zhang, Y. Li, Y. Kuang, J. Song, W. Luo, Y. Wang, Y. Yao, G. Pastel, J. Xie and L. Hu, *Adv. Energy Mater.*, 2017, **7**, 1700595.

S14. J. Oehm, M. KamlAh and V. Knoblauch, *Batteries*, 2023, **9**, 303.

S15. M. Fritsch, G. Standke, C. Heubner, U. Langklotz, A. Michaelis, *J. Energy Storage*, 2018, **16**, 125–132.